Laser Sintering Direct Ink Write Silver Nanoflake Ink for On-Demand Manufacturing of Electronics in Space

Ellie Schlake, *Graduate Student Member, IEEE*, and Nirmala Kandadai, *Senior Member, IEEE*

Abstract— Developing manufacturing methods for flexible electronics will enable and improve the large-scale production of flexible, spatially efficient, and lightweight devices. Laser sintering is a promising postprocessing method to produce consolidated films for flexible electronic devices while reducing power consumption compared to standard thermal sintering. This work further explores laser sintering of direct ink write (nScrypt) printed silver as a continuation of previous studies on nScrypt-printed silver and aerosol jet-printed gold, platinum, and titanium dioxide for manufacturing printed electronics (PEs) on the International Space Station (ISS). Four different laser wavelengths are studied for laser sintering nScrypt silver nanoflake ink on flexible polyimide and rigid glass substrates. The laser systems investigated are continuous wave (CW) 808 nm, CW 445 nm, CW 1064 nm, and pulsed femtosecond (fs) 1040-nm lasers. The laser power and scanning speed are varied to compare the laser systems and optimize laser sintering parameters for the silver ink. The resistivity of the laser-sintered silver NPs is compared to the resistivity of the unsintered silver to demonstrate the effectiveness of laser sintering. An optimal resistivity of 5.81×10^{-8} $\Omega \cdot$m is achieved for the nScrypt silver laser sintered using a fs 1040-nm laser.

Index Terms— Direct ink write, flexible electronics, in-space manufacturing, laser sintering, nScrypt printer, silver.

I. Introduction

PRINTING technologies allow electronic devices to be produced on flexible, thin, cost-effective, and durable substrates [1], [2], [3], [4], [5], [6]. The flexible capabilities of printed electronics (PEs) make them ideal for furthering technology in medical care and consumer electronics, such as biosensors that conform to the user, allowing movement, comfortability, and real-time noninvasive sensing [7], [8], [9]. Direct-deposition printing of nanoparticle (NP) inks, or colloidal suspensions, is the primary process in PE fabrication to produce various electronic device features on flexible substrates [10], [11], [12], [13]. Ink deposition methods include spin coating, inkjet printing (IJP), aerosol jet printing (AJP),

and direct ink writing (DIW) [14], [15], [16]. Spin coating uses centrifugal force to spread the applied ink evenly on the substrate [17]. IJP involves small ink droplets directed from a print head down to the substrate in the desired print pattern [18]. AJP uses aerosolized ink carried by a carrier gas sprayed downward on the substrate, directed, and focused using sheath gas [19]. DIW uses pneumatic or mechanical pressure to extrude the ink onto the substrate [20]. The National Aeronautics and Space Administration (NASA) has an On-Demand Manufacturing of Electronics (ODME) Mission planning to support a DIW nScrypt printer aboard the International Space Station (ISS) to demonstrate 3-D printing capabilities and produce PE devices in space [21]. Unfortunately, printing technologies do not provide a consolidated thin film with the desired material properties [22]; they only deposit the ink as nonconductive clusters suspended in a solvent. A sintering step is required to coalesce the NPs into a film to provide connectivity and achieve the desired film properties [23]. Conventionally, sintering is performed by heat treatment, where the printed sample is placed in a furnace [24]. However, NASA has a power budget of 2200 W aboard the ISS, and the current furnace power consumption exceeds this limitation. A search for a low-power alternative has become essential for NASA's ODME Mission.

Laser sintering is an alternative postprocessing method to sinter printed inks [25], [26], [27], [28], [29]. This process involves exposing the printed film's surface to a laser beam to allow sintering of the NPs to occur. Laser sintering is efficient in enabling high power density to be administered to a small area of the substrate rather than exposing the entire device to high temperatures as thermal and photo sintering methods do [30], [31], [32]. Laser sintering allows for selectivity, as the desired device can be directly written on the printed NP film. The surface of the laser-sintered film is sensitive to various laser parameters, such as laser power, intensity, wavelength, scanning speed, and pulse duration. Moreover, these parameters change with the substrate material, the pretreatment of the substrate, and the ink composition [25]. Early work has investigated laser and sample parameters for laser sintering of spin-coated, IJP, and AJP samples [33], [34], [35], [36], [37], [38], [39], [40].

Essential laser sintering work on silver spin-coated samples was performed by Qin and Watanabe [33] and Theodorakos et al. [34]. Qin and Watanabe [33] laser-sintered spin-coated silver NPs doped with copper (Cu) using a

continuous wave (CW) 1064-nm laser at 5-W power with increased scanning speed. Heat treatment in a furnace was compared to laser sintering results. The furnace-treated samples demonstrated grain growth, but the silver NPs separated into large conglomerates. Laser sintering, however, resulted in a conductive network structure of silver NPs with sheet resistance reduction from 4.45×10^8 to 6.30 Ω/sq. The addition of Cu NPs to silver thin film was studied to improve the homogeneity of the film and the conductivity based on the interaction between the oxidized Cu NPs and a glass substrate. Later, Theodorakos et al. [34] demonstrated laser sintering of spin-coated silver NPs on flexible polyethylene naphthalate (PEN) using three laser systems with wavelengths of 1064 and 532 nm and operating at CW and varying pulse durations (nanoseconds and picoseconds). They found that the CW and nanosecond pulsed laser sintered the silver NPs efficiently but may inflict substrate damage depending on the laser power.

IJP was studied by many researchers, such as Yang et al. [35], Lee et al. [36], Hajjaji et al. [37], and Niittyen et al. [38]. Yang et al. [35] investigated a model of the transient heat transfer and molecular dynamics of laser sintering of metal NPs and laser sintering of IJP silver. The local temperature of the printed silver film increased significantly, but the substrate temperature was much lower, demonstrating laser sintering capabilities on thermal-sensitive substrates. Laser sintering improved with increased laser power and decreased scanning speed; however, the laser power had a more significant effect on sintering than the scanning speed. Therefore, higher speeds can be applied with higher laser power. Lee et al. [36] laser-sintered IJP silver-on-glass samples using a CW 532-nm laser with an elliptical beam shape at different laser intensities. The resistivities of the inkjet silver samples were measured during laser sintering, and the minimum resistivity measured was 3.41×10^{-8} $\Omega \cdot$m. Hajjaji et al. [37] laser-sintered IJP square ring resonator microwave components on polyimide using two different laser sintering patterns. The first pattern traced the structure along the edges with the laser, and the second was a crosshatch pattern. The laser sintering utilized a defocused beam with a diameter of 100 μm and a focused laser beam with a diameter of 50 μm. The laser was a 1080-nm 40-kHz laser with a laser power set between 0 and 20 W. Substrate damage was detected at the lowest power with the focused laser beam. Therefore, laser sintering was performed with a defocused laser beam of 100 μm and a scanning speed of 10 mm/s. The conductivity of the ink was improved from 3.0–5.5 to 6.5–9.5 S/μm after laser sintering. The first sintering pattern was more efficient and resulted in a higher increase in conductivity. In contrast, the second sintering pattern resulted in a more consistent distribution of NPs in the device. Niittyen et al. [38] laser-sintered IJP silver on polycarbonate and polyimide using an 808-nm laser. The laser-sintered samples were compared to furnace-, plasma-, and photonic-sintered samples. Photonic sintering resulted in the most uniform and dense microstructure. Laser sintering was suitable for specific applications in selectively sintering structures, whereas the other methods are better for large-area processing.

In addition, laser sintering of AJP silver samples has been studied [39], [40]. Renn et al. [39] laser-sintered AJP silver by mounting a CW 830-nm fiber-coupled laser output next to the AJP deposition head. As a result, the stages used to create the sample with the AJP were utilized to translate the sample for laser sintering. The laser powers ranged from 100 to 700 mW, and the scanning speed ranged from 5 to 20 mm/s. A 15-cm-long serpentine silver trace was printed on silicone and laser sintered. Laser sintering and elongation tests resulted in a resistance of 9 Ω. Agarwala et al. [40] used laser sintering of AJP samples to develop a flexible strain sensor for wearable at-home health monitoring. The laser-sintered samples on a bandage substrate had a sheet resistance of 0.2 Ω/sq; however, cracking of the substrate was observed. A femtosecond laser with a wavelength of 780 nm was used, and a minimum power of 120 mW to sinter was observed.

We previously studied laser sintering of AJP samples with different NP compositions, such as gold, titanium dioxide, and platinum [41]. Our AJP samples were successfully sintered, resulting in a noticeable decrease in sample resistance (300 kΩ–130 Ω for gold samples) and coalescence of NPs; however, we noticed that as the thickness of the film increased, the laser physics and parameters varied extensively. In addition, laser sintering of nScrypt printed silver was done in our previous work, showing the reduction of resistance of 50–200-μm thick samples from 120.2 to 0.2 Ω. Our preliminary thermal transfer model showed that heat transport varied with thickness and the underlying substrate. In this article, we further study the effect of the thickness of the laser-sintered film, looking specifically into DIW nScrypt-printed silver and the impact of laser parameters and substrate on the sintered film.

Although extensive studies on laser sintering have been conducted, a detailed analysis of laser sintering for DIW nScrypt-printed silver has yet to be done. The printing process of nScrypt printers is distinctly different from that of IJP and AJP, as nScrypt printers use viscous material that is more suitable for its DIW deposition method. The thickness of AJP and IJP samples is sub-micrometer to tens of micrometers, while nScrypt is tens to hundreds of micrometers.

Our work herein presents the results from laser sintering nScrypt printed silver films with varying thicknesses on rigid glass and flexible polyimide substrates in pursuit of NASA's ODME Mission [21]. The experiments were completed using four laser systems, and we show how the laser parameters and the thickness of the samples before laser sintering affect the surface quality and resistivity of laser-sintered films.

II. METHODS

A. Experimental Setup

Laser sintering was performed using four lasers: 1) CW 808-nm diode laser with a 4.6-mm beam diameter; 2) CW 445-nm diode laser with a 9.8-mm beam diameter; 3) CW 1064-nm fiber laser with a 4.5-mm beam diameter; and 4) pulsed fs 1040-nm laser with a 2-mm beam diameter. The experimental setup is organized with the fiber output for each CW laser placed beside
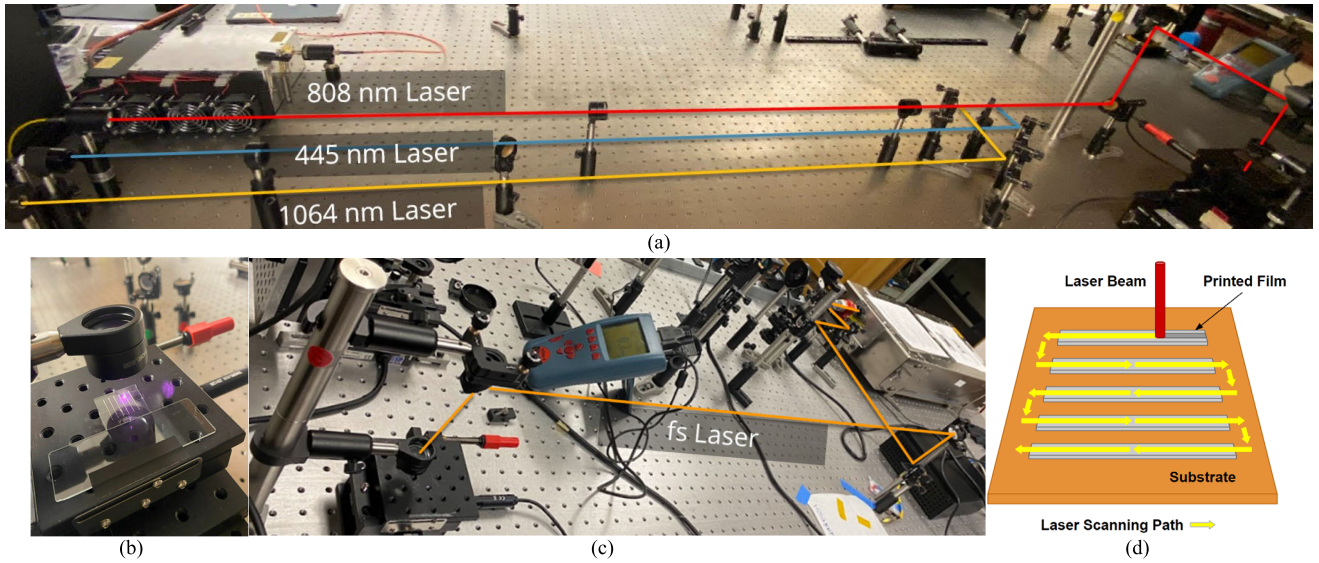
Fig. 1. (a) CW lasers aligned on an optical table directed toward the XYZ-linear stage used for laser sintering experiments. (b) fs laser sintering setup showing a similar XYZ-linear stage used for laser sintering experiments. (c) Silver-on-glass sample placed in the laser sintering experimental setup using a 25.4-mm focusing lens. (d) Diagram of the printing pattern used in laser sintering a silver sample with consecutive printed lines.

each other on an optical table, as shown in Fig. 1(a). The 808- and 445-nm lasers are collimated using plano-convex lenses placed in each beam path. The printed samples are placed on an XYZ-linear motorized stage with the laser beam directed downward and focused on the sample using a 25.4-mm focusing lens, as shown in Fig. 1(b).

Flip mount adapters (Thorlabs) are used at the base of mirror mounts to direct the desired laser wavelength beam to the laser sintering stage. The fs laser is located on a separate optical table with its own XYZ-linear motorized stage and 25.4-mm focusing lens, as shown in Fig. 1(c). Using the 25.4-mm lens, the beams at their focus spot are the following diameters: 1) CW 808-nm laser with a 5.68-μm beam diameter; 2) CW 445-nm diode laser with a 1.47-μm beam diameter; 3) CW 1064-nm fiber laser with a 7.65-μm beam diameter; and 4) pulsed fs 1040-nm laser with a 16.82-μm beam diameter. The sample is translated beneath the focused laser beam to sinter the printed film on the substrate in a linear pattern, as shown in Fig. 1(d). The laser power and scanning speed are varied between the consecutive traces being sintered.

B. Sample Preparation

The silver nanoflake ink was commercially purchased from Novacentrix (HPS-FG77 silver nanoflake (0.3 μm), 85 WT% loading, 65%–90% silver, and 15%–35% diethylene glycol monobutyl ether, butyl carbitol vehicle). The Novacentrix HPS-FG77 silver ink has particles with an average diameter of 300 nm. The samples were printed using the nScript model 150-3Dn-HP Micro-dispense printer and the nScript model 3Dn-Tabletop Micro-dispense printer, as shown in Fig. 2. The silver was printed on glass and polyimide substrates and had two thickness ranges: 10–60 μm and 100–300 μm. The two distinct thicknesses were chosen for specific manufacturing applications on the ISS. The thinner films are considered for traces between components and general circuitry. The thicker films are for filling vias and as a precursor to using
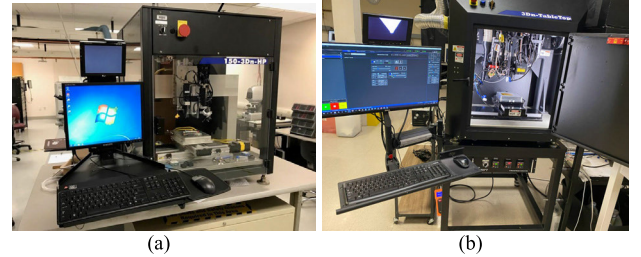
Fig. 2. DIW nScrypt printers used for printing samples. (a) Model 150-3Dn-HP. (b) Model 3Dn-Tabletop.

laser sintering-enabled nScrypt printers to generate on-demand manufacturing of metal parts [42].

C. Measurements and Characterization

The resistance of the sintered traces was measured using a 114-Fluke-digital multimeter using two-point probe IV measurements. To ensure accuracy, random sets of samples were tested using a four-point probe, and the measurements were within a 5% error. Hence, two-point measurements were used throughout this work. The cross-sectional area of the printed samples was calculated with the width and thickness measured using a Tencor Instruments Alpha Step 500 surface profilometer. The resistance and cross-sectional area of the prints were used to calculate the resistivity of the films. The morphology of the traces after laser sintering was imaged using an FEI Teneo field emission scanning electron microscope (SEM).

III. THIN SILVER FILM LASER SINTERING

A. Laser Sintering Using CW Lasers

Four samples of five silver lines on a glass substrate, similar to the sample diagram in Fig. 1(d), were made to test each CW laser system and compare the resulting morphology and resistivity. The thickness of the silver ranged from 49.37 to 58.39 μm. In the power test, the three CW lasers, 445, 808, and 1064 nm, were compared by varying the power of each laser from 1.0 to 2.5 W and keeping the scanning speed at 0.5 mm/s.

808 nm Laser				
Unsintered	1 W	1.5 W	2 W	2.5 W
				200 µm
10.9 Ω-m	3.27×10^{-6} Ω-m	6.44×10^{-7} Ω-m	2.95×10^{-7} Ω-m	2.30×10^{-7} Ω-m

(a)

445 nm Laser				
Unsintered	1 W	1.5 W	2 W	2.5 W
				200 µm
13.1 Ω-m	8.99 Ω-m	0.038 Ω-m	5.31×10^{-5} Ω-m	1.26×10^{-5} Ω-m

(b)

1064 nm Laser				
Unsintered	1 W	1.5 W	2 W	2.5 W
				200 µm
19.0 Ω-m	7.41×10^{-7} Ω-m	3.14×10^{-7} Ω-m	2.34×10^{-7} Ω-m	1.72×10^{-7} Ω-m

(c)

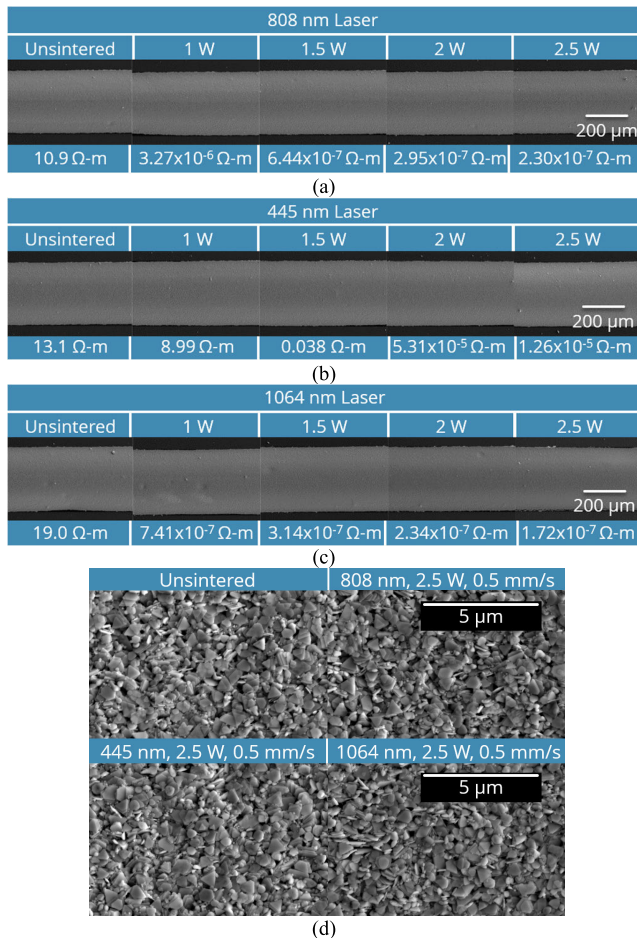| Unsintered	808 nm, 2.5 W, 0.5 mm/s
	5 µm
445 nm, 2.5 W, 0.5 mm/s	1064 nm, 2.5 W, 0.5 mm/s
	5 µm

(d)

Fig. 3. Top-view SEM images of each of the five silver lines on glass using (a) CW 808-nm, (b) CW 445-nm, and (c) CW 1064-nm lasers at 1–2.5 W at 0.5-mm/s scanning speed. (d) 5-µm resolution top-view SEM images of unsintered silver and the fifth line for each CW laser-sintered sample.

Fig. 3(a)–(c) shows the SEM images for laser sintering of silver using the 808-, 445-, and 1064-nm lasers, respectively.

Laser sintering of the thin film silver results in consistent morphology for the three CW lasers at 200-µm resolution, as seen in Fig. 3(a)–(c). The 5-µm resolution SEM images in Fig. 3(d) show the difference in the morphology between the unsintered silver NPs and the silver NPs exposed to the CW lasers. Although the morphology is not differentiable, the resistivity of the films is reduced. The film's resistivity for 445-nm laser-sintered samples decreased from 13.1 to 10^{-5} Ω·m as the power varied from 1.0 to 2.5 W. The 808-nm laser-sintered samples showed a decreased resistivity from 10.9 to 10^{-7} Ω·m. The 1064-nm laser-sintered sample provides a similar resistivity decrease range from 19.0 to 10^{-7} Ω·m. The morphology of each sample is consistent, and there is a reduction in resistivity compared to the unsintered silver for each of the CW lasers used for sintering. The 445-nm laser system had a much higher resistivity than other lasers.

B. Laser Sintering Using the Fs Laser

Fig. 4 shows the SEM images of silver on glass laser-sintered using the fs 1040-nm laser with silver thicknesses ranging from 53.45 to 59.78 µm.

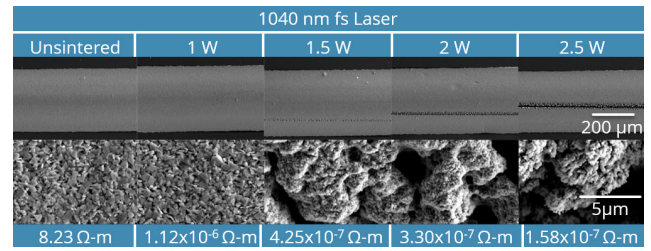| 1040 nm fs Laser				
Unsintered	1 W	1.5 W	2 W	2.5 W
				200 µm
				5µm
8.23 Ω-m	1.12×10^{-6} Ω-m	4.25×10^{-7} Ω-m	3.30×10^{-7} Ω-m	1.58×10^{-7} Ω-m

Fig. 4. SEM images and resistivity of silver Lines 1–5 laser sintered using the fs 1040-nm laser with increased power from 1.0 to 2.5 W and a scanning speed of 0.5 mm/s.

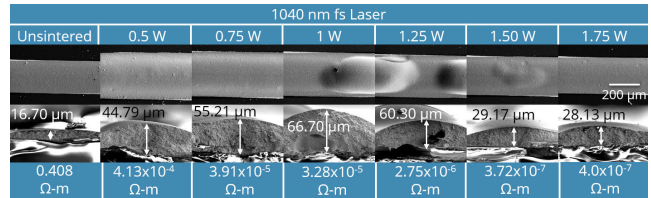| 1040 nm fs Laser						
Unsintered	0.5 W	0.75 W	1 W	1.25 W	1.50 W	1.75 W
						200 µm
16.70 µm	44.79 µm	55.21 µm	66.70 µm	60.30 µm	29.17 µm	28.13 µm
0.408 Ω-m	4.13×10^{-4} Ω-m	3.91×10^{-5} Ω-m	3.28×10^{-5} Ω-m	2.75×10^{-6} Ω-m	3.72×10^{-7} Ω-m	4.0×10^{-7} Ω-m

Fig. 5. Defocused fs laser sintering SEM images and resistivity results with a scanning speed of 0.5 mm/s.

In the first row of SEM images, we observe an ablated line through the silver as laser power increases from 1.0 to 2.5 W. The 5-µm resolution SEM images show increased porosity where the laser beam was in direct contact with the sample and the ablated line was made. However, the silver NPs are no longer individual particles but completely fused across the entire surface. Although the laser exposure resulted in a distinct line across the silver in the laser's incident path, the silver trace's resistivity was reduced due to laser sintering. The resistivity decreased from 8.23 to 10^{-7} Ω·m after laser sintering as the laser power increased.

C. Defocused Laser Beam

A defocused laser beam was tested to reduce the ablation of the silver ink caused by the fs laser. Therefore, thin silver traces with thicknesses ranging from 16.7 to 66.7 µm were printed on glass to test the sintering capabilities of the fs laser when the beam is defocused. To defocus the beam, the sample stage is translated upward 1.6 mm, so the sample is placed above the focal point of the focusing lens and exposed to a less concentrated and larger beam diameter of approximately 1.27 mm instead of 16.8 µm. Fig. 5 shows the SEM images and resistivity of the silver after sintering with the defocused beam for varying thicknesses.

The cross-sectional SEM images show the thickness variation of the printed traces. At higher thicknesses, the surface morphology is lumpier or has a "bubbling effect" compared to the thinner prints when the laser power increases. The thickness where the bubbling effect begins is approximately 60 µm when laser power exceeds 1 W.

The resistivity decreased from 0.408 to 10^{-7} Ω·m after laser sintering using the defocused beam, similar to the focused beam results. Moreover, no silver ablated line is observed when using the defocused beam.

D. Laser Sintering of Silver on a Polyimide Substrate

Polyimide is much less durable to heat penetration than glass but allows for flexibility. The ability to print and laser
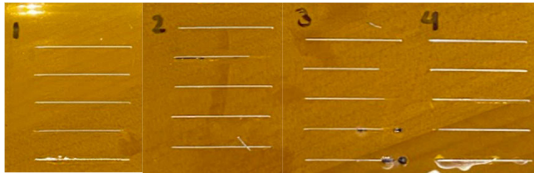
Fig. 6.   Samples 1–4 of five silver nScrypt printed lines on polyimide. The laser wavelengths used for Samples 1–4 are 808, 445, fs 1040, and 1064 nm, respectively.
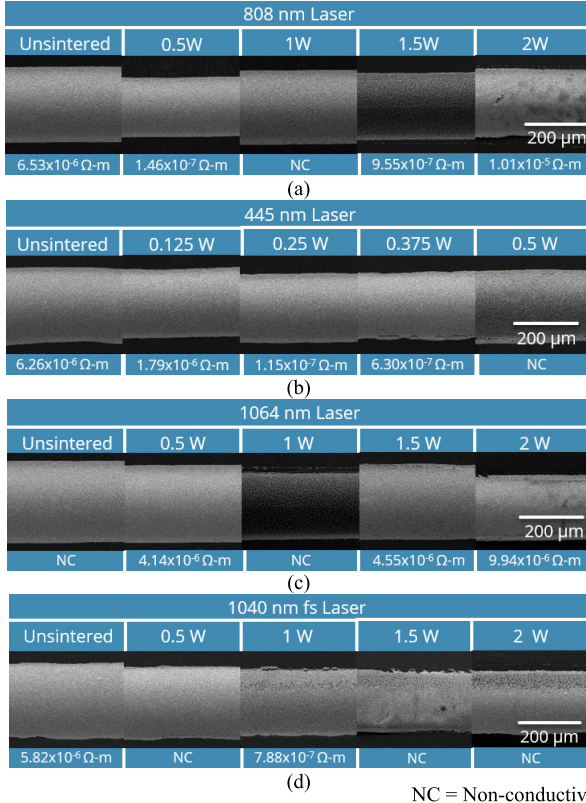

NC = Non-conductive

Fig. 7.   SEM images of silver on polyimide for each silver Line 1–5 using (a) CW 808 nm, (b) CW 445 nm, (c) CW 1064 nm, and (d) fs 1040-nm lasers at 0.5-mm/s scanning speed.

sinter on polyimide is one of the main objectives of this work to achieve flexible electronic capabilities. Fig. 6 shows four silver on polyimide samples, each laser sintered using one of the four laser systems.

The thickness of the samples ranged from 34.60 to 40.80 μm. In Fig. 6, black marks in line with the silver lines indicate where the laser beam caused damage to the polyimide substrate.

Fig. 7 shows samples 1–4 SEM images and resistivities. "Nonconductive" or NC is written in place of the resistivity measurement for nonconductive traces and those that broke off of the substrate before being measured.

The bubbling effect is not present, as the thickness of the samples is maintained below 60 μm. In addition, the resistivity of the unsintered silver was of the magnitude of 10^{-6} Ω·m, unlike previous trials where the unsintered ink was highly resistive. However, resistivity is still reduced after laser sintering with each laser. In a few cases, the silver solidified after being laser sintered and would no longer adhere to the polyimide substrate, resulting in the inability to make resistivity measurements (labeled NC). This was mainly
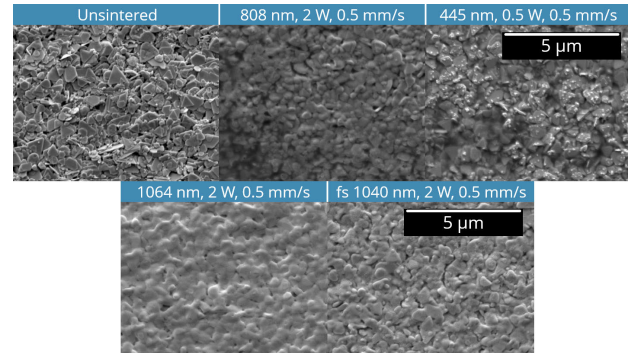

Fig. 8.   Top-view SEM images of unsintered and peeled-off laser-sintered silver on polyimide.
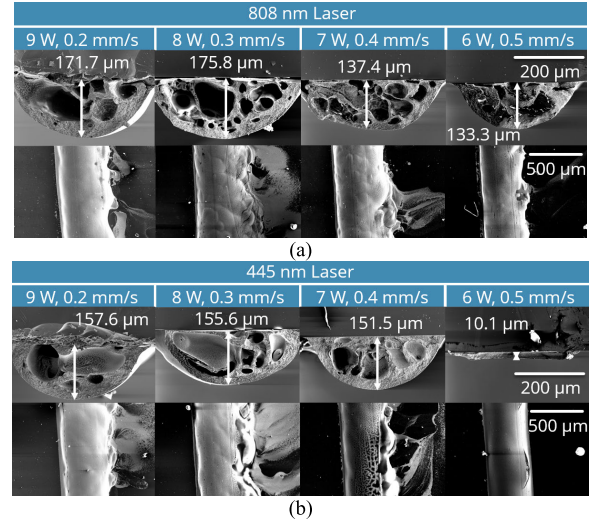
Fig. 9.   Cross-sectional and top-view SEM images of silver laser sintered using (a) 808-nm laser and (b) 445-nm laser at increasing scanning speeds from 0.2 to 0.5 mm/s and decreasing laser power from 9 to 6 W.

observed using the fs laser and at laser powers greater than 0.5 W for CW lasers. We were able to mitigate the effect by sintering at lower powers, as shown by the 445-nm laser. The fs laser was much less stable, resulting in lower adhesion than the CW lasers. However, complete sintering without burning the Kapton was obtained in all the traces when the laser was not directly exposed to the substrate.

Fig. 8 shows a closer inspection of the morphology of the silver on polyimide from Fig. 7. At 5-μm resolution, the coalescence of NPs can be seen for the laser-sintered samples, all of which peeled off of the substrate surface.

The silver was reduced in resistivity, and the bubbling effect was minimized; however, at higher than 0.5 W, the silver peeled off the polyimide. At lower laser power, the silver could adhere and bend with the bending radius of the polyimide substrate.

IV. THICK SILVER FILM LASER SINTERING

A. Spreading of the Silver Film

In this section, we investigated the laser sintering of thick silver films. Fig. 9 shows the cross-sectional SEM images at 200-μm resolution and top-view SEM images at 500-μm resolution of the thick films laser sintered using the 808- and 445-nm lasers. The scanning speed varied from

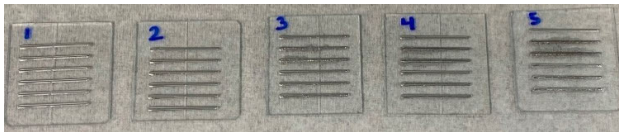Fig. 10. Samples 1–5 of thick silver traces nScrypt printed on glass, each with a different drying condition applied before laser sintering. Sample 1: dried on a hot plate at 80 °C for 5 min. Sample 2: dried on a hot plate at 100 °C for 5 min. Sample 3: dried using the 808-nm laser at 1 W and 0.1-mm/s scanning speed. Sample 4: dried using the 445-nm laser at 1 W and 0.1 mm/s. Sample 5: no drying conditions.

0.2 to 0.5 mm/s, and the laser power varied from 9 to 6 W. The sample thicknesses ranged from 10.10 to 175.80 μm.

The cross-sectional SEM images display the pockets within the silver lines after exposure to the laser. In addition, the top-view SEM images show the spreading of the ink from its displacement from the pockets within the thick prints. The thermal mismatch of the solvent and silver ink particles in the ink causes uneven heating, causing the bubbling and dispersion of the ink. The solvent is not thoroughly evaporated, and much of it is trapped within the film. To overcome this, we investigated a drying step prior to sintering to produce a consistent film for the thick samples.

B. Drying Conditions Prior to Laser Sintering

Five thick nScrypt printed silver-on-glass samples, shown in Fig. 10, were used to test ink drying methods before laser sintering. The thickness of the samples ranged from 83.30 to 180.30 μm. Four samples were dried using four different methods utilizing either a laser or a hot plate, and one sample was kept undried prior to sintering as a control set. Once dried, the samples were each laser sintered using the 808- and 445-nm lasers at 3-W laser power and 0.5-mm/s scanning speed.

Fig. 11 shows the SEM images of the five silver-on-glass samples, along with the drying conditions and resistivities for each print. Fig. 11(a) shows the morphology and resistivity for the silver Line 2 results for each of Samples 1–5 using the 808-nm laser for laser sintering. Similarly, Fig. 11(b) shows the results for the silver Line 5 for each of Samples 1–5 laser sintered using the 445-nm laser. The first column describes the sample drying conditions before laser sintering. The second and third columns show the 500- and 5-μm resolution SEM images of the top-view surface morphology, respectively. The fourth and fifth columns show the 200- and 10-μm resolution SEM images of the cross sections of the silver traces, respectively. The sixth, far right column entries are the resistivities of the trace.

The first row of Fig. 11(a) and (b) shows the results of laser sintering after drying the silver using a hot plate at 80 °C for 5 min. The surface and cross-sectional morphology show the consolidated film with a smooth film and resistivity reduction from nonconductive to 10^{-4} Ω·m. The second row of SEM images shows the results of the sample dried on a hot plate at 100 °C for 5 min. Similar to Sample 1, the morphology of the film is smooth, and the resistivity is 10^{-4} Ω·m. SEM images in rows 3–5 show Samples 3–5 morphology. The top-view and cross-sectional view SEM images show the present bubbling effect. The traces that were dried by laser exposure in Samples
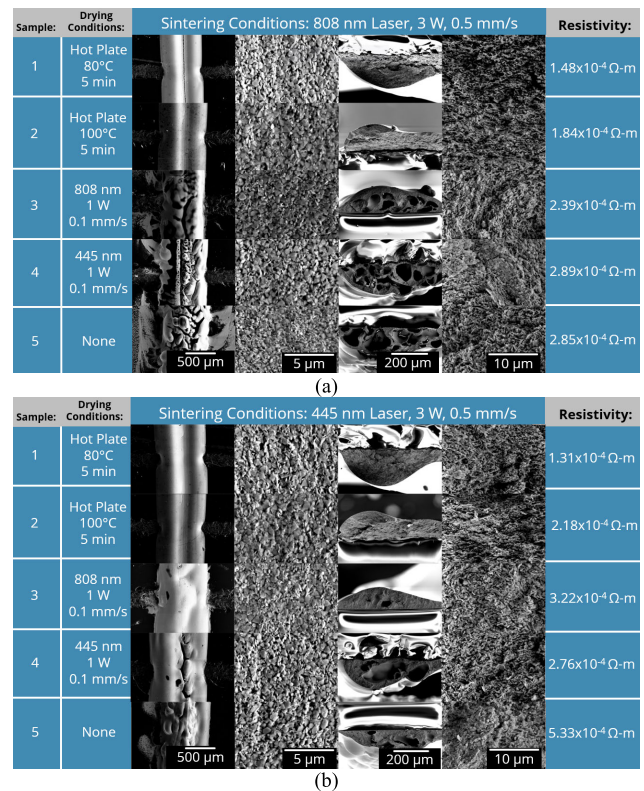
Fig. 11. (a) SEM images and resistivity for Line 2 of Samples 1–5 after laser sintering using the 808-nm laser at 3-W power and 0.5-mm/s scanning speed after each drying condition. (b) SEM images and resistivity for Line 5 of Samples 1–5 laser sintered using the 445-nm laser at 3-W power and 0.5-mm/s scanning speed after each drying condition.

4 and 5 reduced ink spreading compared to Sample 5, which had no drying prior to sintering.

Although each sample, regardless of the drying method, resulted in the same magnitude of resistivity, drying the silver samples with the hot plate resulted in the most consistent film morphology. The 808-nm laser and the 445-nm lasers used for laser sintering resulted in similar resistivity; however, the morphology of the 445-nm laser-sintered films in Fig. 11(b) had a smoother film than the film laser sintered using 808 nm shown in Fig. 11(a).

C. Scanning Speed and Substrate Comparison

To determine a more consistent film quality, the effect of the scanning speed on laser sintering to achieve the desired film morphology and characteristics was investigated. The scanning speed was increased from 0.1 to 1.5 mm/s, and the laser power and wavelength were kept constant at 3 W and 1064 nm, respectively. Fig. 12 shows the SEM images and resistivities due to varying scanning speeds used on silver printed on glass and polyimide. The samples were dried on a hot plate at 100 °C for 10 min prior to laser sintering. Fig. 12 displays how the bubbling effect becomes more prevalent as the scanning speed increases. With a slower scanning speed, the ink is exposed to the laser longer, and the solvent left in the ink can uniformly heat and evaporate, unlike during more rapid exposure. Therefore, at slower speeds, a more desired film is achieved. The sample on a polyimide substrate resulted in peeling off of the silver at speeds higher than

1064 nm Laser, Glass Substrate									
Unsintered	0.1 mm/s	0.4 mm/s	0.7 mm/s	1.0 mm/s	1.3 mm/s	1.6 mm/s	1.9 mm/s	2.2 mm/s	2.5 mm/s
23.9 MΩ	0.3 Ω	0.2 Ω	0.3 Ω	0.2 Ω	0.3 Ω	1.8 MΩ	0.4 Ω	2 kΩ	0.6 Ω

(a)

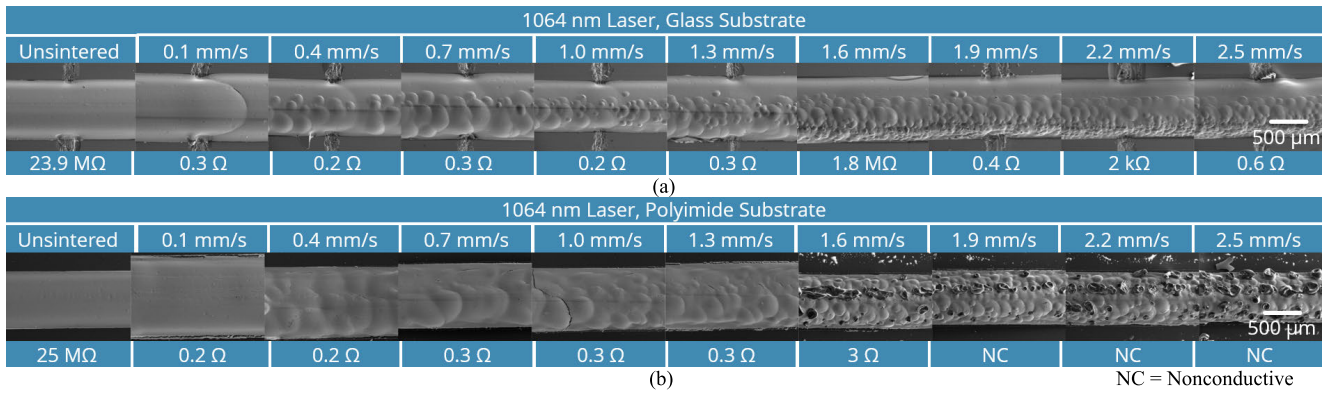| 1064 nm Laser, Polyimide Substrate									
Unsintered	0.1 mm/s	0.4 mm/s	0.7 mm/s	1.0 mm/s	1.3 mm/s	1.6 mm/s	1.9 mm/s	2.2 mm/s	2.5 mm/s
25 MΩ	0.2 Ω	0.2 Ω	0.3 Ω	0.3 Ω	0.3 Ω	3 Ω	NC	NC	NC

(b)

NC = Nonconductive

Fig. 12. Top-view SEM images of silver after laser sintering with the 1064-nm laser at 3 W using varying scanning speeds on (a) glass substrate and (b) polyimide substrate.

808 nm Laser					
Unsintered	0.2 mm/s	0.5 mm/s	0.8 mm/s	1.1 mm/s	1.4 mm/s
14 MΩ	0.2 Ω	0.2 Ω	0.2 Ω	0.2 Ω	0.2 Ω

(a)

1064 nm Laser					
Unsintered	0.2 mm/s	0.5 mm/s	0.8 mm/s	1.1 mm/s	1.4 mm/s
14.4 MΩ	0.2 Ω	0.4 Ω	0.4 Ω	0.5 Ω	0.3 Ω

(b)

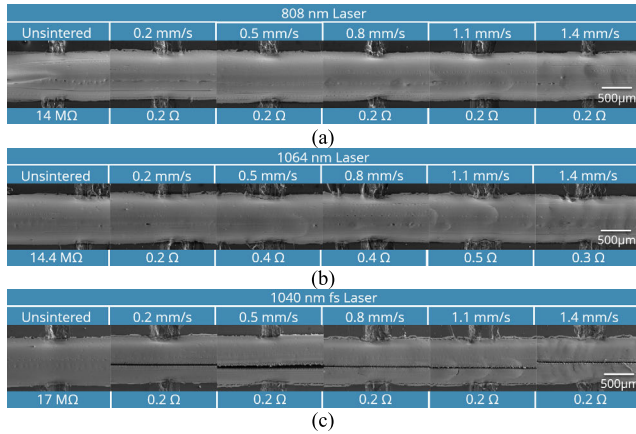| 1040 nm fs Laser					
Unsintered	0.2 mm/s	0.5 mm/s	0.8 mm/s	1.1 mm/s	1.4 mm/s
17 MΩ	0.2 Ω	0.2 Ω	0.2 Ω	0.2 Ω	0.2 Ω

(c)

Fig. 13. Scanning speed comparison from 0.2 to 1.4 mm/s for (a) CW 808-nm, (b) CW 1064-nm, and (c) 1040-nm fs lasers used at 5 W for CW lasers and 3 W for the fs laser.

(a)

Unsintered	fs Laser, 3 W, 0.2 mm/s

(b)

Fig. 14. Close-up top-view SEM images of silver on glass from Fig. 13(c). (a) fs laser ablated line using 3-W power at 0.2-mm/s scanning speed at 30-μm resolution. (b) 4-μm resolution of unsintered silver and fs laser-sintered silver ablated line edge using 3 W and 0.2-mm/s scanning speed.

1.6 mm/s, resulting in the NC labeling for resistivity. The slower scanning speeds resulted in flexible silver on polyimide.

Silver on glass was again compared by laser sintering at varying scanning speeds and using different laser wavelengths, as shown in Fig. 13. The silver was dried on a hot plate at 100 °C for 5 min and then air-dried for over 24 h, resulting in a completely dried thick film. The CW 808-nm, CW 1064-nm, and fs 1040-nm lasers were used to sinter the silver at increasing scanning speeds from 0.2 to 1.4 mm/s. The laser power for the CW 808- and 1064-nm lasers was maintained at 5 W, while the fs laser was at 3 W for each change in scanning speed.

The bubbling effect is kept minimal with the extended drying time of the samples; however, the 3-W power and focus of the fs laser resulted in an ablated line through the sample regardless of the scanning speed. The resistance of the traces was reduced from the unsintered silver for each laser wavelength from MΩ to < 0.5 Ω. Although the fs laser ablated the silver, the entire trace was sintered, and the resulting resistances were similar to those of the CW lasers.

Fig. 14 shows the close-up SEM images of the ablated line in the silver made by the fs laser at 30- and 4-μm resolution. Fig. 14(a) shows the span of the ablated line through the silver using 3-W power and 0.2-mm/s scanning speed. The width of the gap is approximately 45 μm at the surface of the sample and reduces to nearly 8 μm at the area deeper into the silver but still visible. Fig. 14(b) shows the side-

by-side 4-μm resolution images of unsintered silver to fs laser-sintered silver at 3 W and 0.2-mm/s scanning speed. The flakes of the unsintered silver are replaced with conglomerated silver.

D. Laser Wavelength and Power Comparison

Silver traces with 200–240-μm thickness were printed on glass and dried on a hot plate at 100 °C for 5 min before being laser sintered using the 1064-nm laser. Previously, drying using a hot plate prior to laser sintering reduced the bubbling effect of the film; however, the laser power was maintained at 3 W for sintering.

A range of laser powers of 1.0–5.5 W with a 1064-nm laser with a scanning speed of 0.5 mm/s was used to sinter. Fig. 15 shows the silver's top-view and cross-sectional SEM images after laser sintering with the 1064-nm laser at a scanning speed of 0.5 mm/s. In Fig. 15, SEM images display the reliance on laser power for the resulting surface and cross-sectional morphology. As the laser power increases, the bubbling effect increases. Although the bubbling effect increases, the resistivity is reduced from unsintered 10^{-4} to 10^{-6} Ω·m.

1064 nm Laser										
Unsintered	1 W	1.5 W	2 W	2.5 W	3 W	3.5 W	4 W	4.5 W	5 W	5.5W
4.16x10⁻⁴ Ω-m	3.62x10⁻⁵ Ω-m	7.53x10⁻⁶ Ω-m	1.31x10⁻⁵ Ω-m	1.99x10⁻⁶ Ω-m	2.63x10⁻⁵ Ω-m	1.19x10⁻⁶ Ω-m	1.06x10⁻⁶ Ω-m	1.27x10⁻⁶ Ω-m	1.34x10⁻⁶ Ω-m	9.41x10⁻⁷ Ω-m

Fig. 15. Top and cross-sectional SEM images of silver on glass dried using a hot plate at 100 °C for 5 min and laser sintered using the 1064-nm laser at a 0.5-mm/s scanning speed as the laser power increases from 1 to 5.5 W.

808 nm Laser					
Unsintered	3.5 W	4 W	4.5 W	5 W	5.5 W
5.17x10⁻⁵ Ω-m	1.79x10⁻⁶ Ω-m	1.41x10⁻⁶ Ω-m	9.12x10⁻⁷ Ω-m	4.80x10⁻⁷ Ω-m	5.59x10⁻⁷ Ω-m

(a)

445 nm Laser					
Unsintered	3.5 W	4 W	4.5 W	5 W	5.5 W
2.53x10⁻⁵ Ω-m	1.25x10⁻⁵ Ω-m	2.07x10⁻⁶ Ω-m	4.00x10⁻⁶ Ω-m	2.15x10⁻⁶ Ω-m	2.06x10⁻⁶ Ω-m

(b)

Fig. 16. Top and cross-sectional SEM images of silver on glass dried using a hot plate at 100 °C for 5 min and laser sintered using (a) 808- and (b) 445-nm lasers at a 0.5-mm/s scanning speed as laser power increases from 3.5 to 5.5 W.

TABLE I

EDS SPECTRUM RESULTS

Spectrum	Ag (Wt%)	C (Wt%)	O (Wt%)
1	83.2	11.0	5.8
2	91.7	5.0	3.3
3	0	74.6	25.4

Fig. 17. EDS scanned image of silver sample surface after laser sintering with the 808-nm laser at 7.5-W power and 0.5-mm/s scanning speed. The three spectrum measurement areas are indicated with arrow labels.

To compare to the 1064-nm laser, the 808- and 445-nm lasers were used to sinter the thick silver on glass prints after drying on a hot plate at 100 °C for 5 min. The morphology and resistivity are shown in Fig. 16.

The bubbling effect is present for the three CW lasers used; however, the 445-nm laser-sintered silver at 3.5 W generated a smooth film morphology, which was not present with 1064- and 808-nm results. This may be due to the decreased interplay between the substrate and the laser heating the film, whereas for thinner films, the laser is absorbed by the substrate along with the ink itself [1].

E. Further Investigation of the Bubbling Effect

Finally, given the breakage of the film, we wanted to identify what caused the film to bubble. We performed energy-dispersive spectroscopy (EDS) to determine the composition of uneven morphology of the silver films observed at high speeds and high power. The EDS image and areas scanned are shown in Fig. 17.

As described in Table I, the concentration of carbon and oxygen increased, and the concentration of silver decreased as the areas in Fig. 17 became darker. There is minimal oxidation of the surface of the silver until the solid black areas where the bubbling is occurring. Carbon and oxygen are present in those areas, but no silver is detected. The bubbles are from the monobutyl ether solvent made of carbon, hydrogen, and oxygen bubbling at the surface after heating through laser exposure.

V. CONCLUSION

The absorption cross section of silver NPs peaks at ~430 nm; however, the peak absorption wavelength increases as the NP size increases [43]. The ink studied in this work has an average NP diameter of approximately 300 nm, where the 430-nm peak value is for NPs with diameters below 50 nm. Therefore, the longer laser wavelengths perform better for laser sintering the silver NPs in this study than the 445-nm laser. In addition, depending on the thickness of the printed film, the laser wavelength that performed the best changes due to the interplay of the substrate in the absorbance of the laser light. The magnitude of the best resistivity resulting from each laser system for thick and thin silver traces is shown in Table II.

For the thick silver, the CW lasers at 808- and 1064-nm wavelengths resulted in the lowest overall resistivities of magnitude 10^{-7} Ω·m. The CW 445 nm and fs laser had similar peak performances, with a magnitude of 10^{-6} Ω·m. For thin silver, the fs laser performed best with a magnitude of 10^{-8} Ω·m resistivity. Moreover, the CW 808- and 1064-nm lasers performed better than the 445-nm laser, with a resistivity of magnitude 10^{-7} Ω·m.

For thin silver samples, the morphology of each sample using CW lasers is consistent and does not result in ink
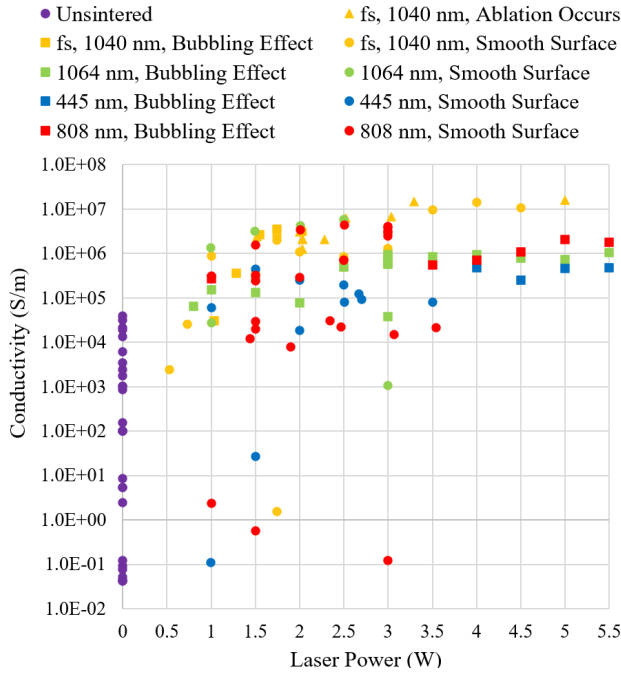
Fig. 18. Conductivity and morphology summary of silver laser sintered with varying wavelengths and laser powers at 0.5-mm/s scanning speed.

TABLE II
LOWEST RESISTIVITY FOR EACH LASER SYSTEM

Laser System	Thin Silver (10-60 μm) Resistivity (Ω·m)	Thick Silver (100-300 μm) Resistivity (Ω·m)
CW 445 nm	2.27×10^{-6}	1.25×10^{-6}
CW 808 nm	2.43×10^{-7}	4.80×10^{-7}
CW 1064 nm	1.72×10^{-7}	9.41×10^{-7}
fs 1040 nm	5.81×10^{-8}	1.04×10^{-6}

spreading or bubbling. The fs laser results in the ablation of the ink where it is directly exposed to the focused laser beam. Defocusing the fs laser beam mitigates the ablating effect; however, bubbling in the ink can be observed at thicknesses greater than 60 μm. When the thickness of the silver film exceeds $\sim$60 μm, the ink's solvent does not evaporate adequately through laser sintering, causing bubbling and carbon deposits on the surface. The bubbling effect of thicker samples on either glass or polyimide worsens when higher laser powers and scanning speeds are used. The 808- and 1064-nm lasers do well for either thick or thin silver prints in reducing resistivity compared to the 445-nm laser; however, the 445-nm laser is more consistent in reducing the bubbling effect in the film and generating a smooth film for thicker films.

For polyimide substrates rather than glass, regardless of the laser system used for laser sintering, powers higher than 0.5 W and scanning speeds higher than 1.6 mm/s cause the sintered silver to fall off due to its poor flexibility and lack of adhesion at its solidified state. However, using laser powers lower than 0.5 W and at slower speeds, the silver adhered to the surface. These samples remained intact with the flexibility of the polyimide while still improving in conductivity. The substrate and ink thickness play a significant role in the laser power needed for adequate laser sintering. A detailed investigation of our original model [41] using COMSOL software [44] to study the effect of the substrate and film thickness is required.
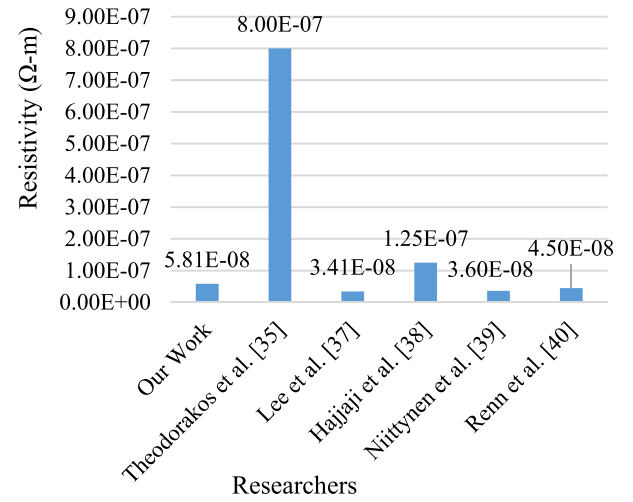
Fig. 19. Resistivity comparison between our laser sintering work on DIW nScrypt silver and previous laser sintering work on spin-coated [34], IJP [36], [37], [38], and AJP [39] silver.

Fig. 18 shows the compilation of laser sintering trials varying the laser power using different laser wavelengths at 0.5-mm/s scanning speed. The silver resistivity is plotted along with its morphology after laser sintering. The desired, smooth surface is indicated by the circular data points in the plot. Notice that the resistivity is plotted logarithmically to easily show the change in magnitude between the unsintered and laser-sintered films.

The minimum resistivity (Ω·m) is shown in Fig. 19, comparing our laser sintering work for DIW nScrypt printed silver to previously studied laser sintering of spin-coated, IJP, and AJP silver. In our work, the optimal thin silver samples' resistivity is 5.81×10^{-8} Ω·m. We showcase that our values are the same or lower order of magnitude than those generated by other groups.

In our work, we successfully showcase that the film morphology and, subsequently, the film's resistivity can be controlled with laser parameters such as wavelengths, power, and speed.

REFERENCES

[1] J. A. Rogers, T. Someya, and Y. Huang, "Materials and mechanics for stretchable electronics," *Science*, vol. 327, no. 5973, pp. 1603–1607, Mar. 2010, doi: 10.1126/science.1182383.

[2] Y. Zheng, Z. He, Y. Gao, and J. Liu, "Direct desktop printed-circuits-on-paper flexible electronics," *Sci. Rep.*, vol. 3, no. 1, May 2013, Art. no. 1, doi: 10.1038/srep01786.

[3] W. S. Wong and A. Salleo, *Flexible Electronics: Materials and Applications*. Cham, Switzerland: Springer, 2009.

[4] D. Corzo, G. Tostado-Blázquez, and D. Baran, "Flexible electronics: Status, challenges and opportunities," *Frontiers Electron.*, vol. 1, Sep. 2020, Art. no. 594003. [Online]. Available: https://www.frontiersin.org/articles/10.3389/felec.2020.594003

[5] *Highly Conductive, Flexible, Polyurethane-Based Adhesives for Flexible and Printed Electronics-Li-2013-Advanced Functional Materials-Wiley Online Library*. Accessed: Jan. 18, 2024. [Online]. Available: https://onlinelibrary.wiley.com/doi/abs/10.1002/adfm.201202249?casa_token=bfQjxFA5c5gAAAAA:pPr7lz3AF5E68x5zLmusqk20gnw160FUYHMU7_IO66F2bS6UORPZBXTLvAqV-v0BQUXcZMs-mdQ34Oo

[6] Y. Bonnassieux et al., "The 2021 flexible and printed electronics roadmap," *Flexible Printed Electron.*, vol. 6, no. 2, May 2021, Art. no. 023001, doi: 10.1088/2058-8585/abf986.

[7] A. Koh et al., "A soft, wearable microfluidic device for the capture, storage, and colorimetric sensing of sweat," *Sci. Transl. Med.*, vol. 8, no. 366, Nov. 2016, Art. no. 366ra165, doi: 10.1126/scitranslmed.aaf2593.

[8] W. Gao, H. Ota, D. Kiriya, K. Takei, and A. Javey, "Flexible electronics toward wearable sensing," *Accounts Chem. Res.*, vol. 52, no. 3, pp. 523–533, Mar. 2019, doi: 10.1021/acs.accounts.8b00500.

[9] Y. Yang and W. Gao, "Wearable and flexible electronics for continuous molecular monitoring," *Chem. Soc. Rev.*, vol. 48, no. 6, pp. 1465–1491, 2019, doi: 10.1039/C7CS00730B.

[10] M. Zeng and Y. Zhang, "Colloidal nanoparticle inks for printing functional devices: Emerging trends and future prospects," *J. Mater. Chem. A*, vol. 7, no. 41, pp. 23301–23336, 2019, doi: 10.1039/c9ta07552f.

[11] Y. Zhang et al., "Ink formulation, scalable applications and challenging perspectives of screen printing for emerging printed microelectronics," *J. Energy Chem.*, vol. 63, pp. 498–513, Dec. 2021, doi: 10.1016/j.jechem.2021.08.011.

[12] P. M. Grubb, H. Subbaraman, S. Park, D. Akinwande, and R. T. Chen, "Inkjet printing of high performance transistors with micron order chemically set gaps," *Sci. Rep.*, vol. 7, no. 1, p. 1202, Apr. 2017, doi: 10.1038/s41598-017-01391-2.

[13] H. Subbaraman et al., "Inkjet-printed two-dimensional phased-array antenna on a flexible substrate," *IEEE Antennas Wireless Propag. Lett.*, vol. 12, pp. 170–173, 2013.

[14] H. Zhang, S. K. Moon, and T. H. Ngo, "3D printed electronics of non-contact ink writing techniques: Status and promise," *Int. J. Precis. Eng. Manuf.-Green Technol.*, vol. 7, no. 2, pp. 511–524, Mar. 2020, doi: 10.1007/s40684-019-00139-9.

[15] Y. Han, Y. Cui, X. Liu, and Y. Wang, "A review of manufacturing methods for flexible devices and energy storage devices," *Biosensors*, vol. 13, no. 9, p. 896, Sep. 2023, doi: 10.3390/bios13090896.

[16] S. M. F. Cruz, L. A. Rocha, J. C. Viana, S. M. F. Cruz, L. A. Rocha, and J. C. Viana, "Printing technologies on flexible substrates for printed electronics," in *Flexible Electronics*. London, U.K.: IntechOpen, 2018, doi: 10.5772/intechopen.76161.

[17] N.-T. Nguyen, "Fabrication technologies," in *Micromixers*, 2nd ed., N.-T. Nguyen, Ed. Oxford, U.K.: William Andrew Publishing, 2012, pp. 113–161, doi: 10.1016/B978-1-4377-3520-8.00004-8.

[18] A. Bastola et al., "Formulation of functional materials for inkjet printing: A pathway towards fully 3D printed electronics," *Mater. Today Electron.*, vol. 6, Dec. 2023, Art. no. 100058, doi: 10.1016/j.mtelec.2023.100058.

[19] E. B. Secor, "Principles of aerosol jet printing," *Flexible Printed Electron.*, vol. 3, no. 3, Jul. 2018, Art. no. 035002, doi: 10.1088/2058-8585/aace28.

[20] Z. Hou, H. Lu, Y. Li, L. Yang, and Y. Gao, "Direct ink writing of materials for electronics-related applications: A mini review," *Frontiers Mater.*, vol. 8, Apr. 2021, Art. no. 647229. [Online]. Available: https://www.frontiersin.org/articles/10.3389/fmats.2021.647229

[21] *In Space Manufacturing—On Demand Manufacturing Electronics (ISM-ODME)*. NASA TechPort. Accessed: Jan. 23, 2024. [Online]. Available: https://techport.nasa.gov/view/116412

[22] C. Cano-Raya, Z. Z. Denchev, S. F. Cruz, and J. C. Viana, "Chemistry of solid metal-based inks and pastes for printed electronics—A review," *Appl. Mater. Today*, vol. 15, pp. 416–430, Jun. 2019, doi: 10.1016/j.apmt.2019.02.012.

[23] R. M. German, "Thermodynamics of sintering," in *Sintering of Advanced Materials*, Z. Z. Fang, Ed. Cambridge, U.K.: Woodhead Publishing, 2010, pp. 3–32, doi: 10.1533/9781845699949.1.3.

[24] F. M. Pinto, R. C. Silva, and F. A. La Porta, "2. Overview of conventional and unconventional sintering Methods–Knovel," in *Green Sustainable Process for Chemical and Environmental Engineering and Science*. Amsterdam, The Netherlands: Elsevier, 2022, pp. 15–35.

[25] J. Noh, J. Ha, and D. Kim, "Femtosecond and nanosecond laser sintering of silver nanoparticles on a flexible substrate," *Appl. Surf. Sci.*, vol. 511, May 2020, Art. no. 145574, doi: 10.1016/j.apsusc.2020.145574.

[26] E. Mayer, T. Stichel, S. Roth, S. Neermann, J. Franke, and M. Schmidt, "Generation of printed electronics on thermal sensitive substrates by laser assisted sintering of nanoparticle inks," in *Proc. 14th Int. Congr. Molded Interconnect Devices (MID)*, Amberg, Germany, Feb. 2021, pp. 1–7, doi: 10.1109/MID50463.2021.9361625.

[27] A. J. Lopes, I. H. Lee, E. MacDonald, R. Quintana, and R. Wicker, "Laser curing of silver-based conductive inks for in situ 3D structural electronics fabrication in stereolithography," *J. Mater. Process. Technol.*, vol. 214, no. 9, pp. 1935–1945, Sep. 2014, doi: 10.1016/j.jmatprotec.2014.04.009.

[28] O. Ermak, M. Zenou, G. B. Toker, J. Ankri, Y. Shacham-Diamand, and Z. Kotler, "Rapid laser sintering of metal nano-particles inks," *Nanotechnology*, vol. 27, no. 38, Sep. 2016, Art. no. 385201, doi: 10.1088/0957-4484/27/38/385201.

[29] E. Balliu, H. Andersson, M. Engholm, T. Öhlund, H.-E. Nilsson, and H. Olin, "Selective laser sintering of inkjet-printed silver nanoparticle inks on paper substrates to achieve highly conductive patterns," *Sci. Rep.*, vol. 8, no. 1, Jul. 2018, Art. no. 10408, doi: 10.1038/s41598-018-28684-4.

[30] E. M. Heckman, C. M. Bartsch, E. B. Kreit, R. S. Aga, and F. Ouchen, "Printed electronics for aerospace applications," in *Women in Aerospace Materials*, M. E. Kinsella, Ed. Cham, Switzerland: Springer, 2020, pp. 93–104, doi: 10.1007/978-3-030-40779-7_7.

[31] R. S. Aga, E. B. Kreit, S. R. Dooley, C. M. Bartsch, E. M. Heckman, and R. S. Aga, "Considerations in printing conductive traces for high pulsed power applications," *Microelectron. Rel.*, vol. 81, pp. 342–351, Feb. 2018, doi: 10.1016/j.microrel.2017.10.037.

[32] D. S. B. Heidary, M. Lanagan, and C. A. Randall, "Contrasting energy efficiency in various ceramic sintering processes," *J. Eur. Ceram. Soc.*, vol. 38, no. 4, pp. 1018–1029, Apr. 2018, doi: 10.1016/j.jeurceramsoc.2017.10.015.

[33] G. Qin and A. Watanabe, "Conductive network structure formed by laser sintering of silver nanoparticles," *J. Nanoparticle Res.*, vol. 16, no. 11, p. 2684, Nov. 2014, doi: 10.1007/s11051-014-2684-8.

[34] I. Theodorakos, F. Zacharatos, R. Geremia, D. Karnakis, and I. Zergioti, "Selective laser sintering of Ag nanoparticles ink for applications in flexible electronics," *Appl. Surf. Sci.*, vol. 336, pp. 157–162, May 2015, doi: 10.1016/j.apsusc.2014.10.120.

[35] Y. Yang, Z. Li, S. Yang, Y. Li, and J. Huang, "Multiscale simulation study of laser sintering of inkjet-printed silver nanoparticle inks," *Int. J. Heat Mass Transf.*, vol. 159, Oct. 2020, Art. no. 120110, doi: 10.1016/j.ijheatmasstransfer.2020.120110.

[36] D. G. Lee, D. K. Kim, Y. J. Moon, and S.-J. Moon, "Effect of laser-induced temperature field on the characteristics of laser-sintered silver nanoparticle ink," *Nanotechnology*, vol. 24, no. 26, Jul. 2013, Art. no. 265702, doi: 10.1088/0957-4484/24/26/265702.

[37] C. E. Hajjaji et al., "Optimizing the conductivity of ink-jet printed microwave components on polymer substrates by laser sintering," in *Proc. 49th Eur. Microw. Conf. (EuMC)*, Oct. 2019, pp. 778–781, doi: 10.23919/EUMC.2019.8910768.

[38] J. Niittynen, R. Abbel, M. Mäntysalo, J. Perelaer, U. S. Schubert, and D. Lupo, "Alternative sintering methods compared to conventional thermal sintering for inkjet printed silver nanoparticle ink," *Thin Solid Films*, vol. 556, pp. 452–459, Apr. 2014, doi: 10.1016/j.tsf.2014.02.001.

[39] M. J. Renn, M. Schrandt, J. Renn, and J. Q. Feng, "Localized laser sintering of metal nanoparticle inks printed with aerosol Jet technology for flexible electronics," *J. Microelectron. Electron. Packag.*, vol. 14, no. 4, pp. 132–139, Oct. 2017, doi: 10.4071/imaps.521797.

[40] S. Agarwala et al., "Wearable bandage-based strain sensor for home healthcare: Combining 3D aerosol jet printing and laser sintering," *ACS Sensors*, vol. 4, no. 1, pp. 218–226, Jan. 2019, doi: 10.1021/acssensors.8b01293.

[41] E. Schlake, J. Corona, and N. Kandadai, "Laser sintering of various film compositions used in flexible printed electronics," in *Proc. IEEE Int. Flexible Electron. Technol. Conf. (IFETC)*, San Jose, USA, CA, USA, Aug. 2023, pp. 1–3, doi: 10.1109/IFETC57334.2023.10254881.

[42] *In Space Manufacturing—On Demand Manufacturing Metal (ISM-ODMM)*. NASA TechPort. Accessed: Jan. 23, 2024. [Online]. Available: https://techport.nasa.gov/view/116259

[43] nanoComposix. *Silver Nanoparticles: Optical Properties*. nanoComposix. Accessed: Jan. 24, 2024. [Online]. Available: https://nanocomposix.com/pages/silver-nanoparticles-optical-properties

[44] *COMSOL: Multiphysics Software for Optimizing Designs*. COMSOL. Accessed: Jan. 24, 2024. [Online]. Available: https://www.comsol.com/